https://ijac.journals.pnu.ac.ir/

Iranian Journal of Analytical Chemistry

Volume 13, Issue 1, Spring 2026, Pages 151-172

DOI: 10.30473/ijac.2026.80202.1364

Research Article

Enhancing Photocatalytic Performance: Application of PPS/PVA/Fe_3O_4/AgNPs Nanocomposites for the Efficient Degradation of Methyl Orange

Akram Afshari Kaveh[1], Sheida Ahmadi[2*] ✉

1. Ph.D. Student, Department of Chemistry, Payame Noor University, Tehran, Iran
2. Associate Prof., Department of Chemistry, Payame Noor University, Tehran, Iran.

✉ **Correspondence:**
Sheida Ahmadi
Email: sh.ahmadi_ch@pnu.ac.ir

Received: 11 Nov 2026
Accepted: 14 Nov 2026

How to cite
A. Afshari Kaveh & Sh. Ahmadi, Enhancing Photocatalytic Performance: Application of PPS/PVA/Fe_3O_4/AgNPs Nanocomposites for the Efficient Degradation of Methyl Orange, *Iran. J. Anal. Chem*. 13 (2026) 151-172. (DOI:10.30473/ijac.2026.80202.1364)

A B S T R A C T

In this study, a PPS/PVA/Fe_3O_4/AgNPs nanocomposite was prepared by a simple co-precipitation method and investigated as a visible-light-responsive photocatalyst for the degradation of methyl orange (MO) in aqueous solution. The prepared materials were characterized using X-ray diffraction (XRD), Fourier-transform infrared spectroscopy (FT-IR), energy-dispersive X-ray spectroscopy (EDX), vibrating sample magnetometry (VSM), Brunauer–Emmett–Teller (BET) analysis, field-emission scanning electron microscopy (FESEM), and dynamic light scattering (DLS). The FESEM images were used for qualitative evaluation of surface morphology, while DLS was employed to measure the hydrodynamic diameter of the samples in suspension. The BET surface area increased from 1.52 $m^2\ g^{-1}$ for PPS to 26.68 $m^2\ g^{-1}$ for the PPS/PVA/Fe_3O_4/AgNPs nanocomposite. Under the applied experimental conditions, the nanocomposite achieved approximately 91% MO degradation after 120 min of visible-light irradiation, with an apparent pseudo-first-order rate constant (k_app) of $9.1 \times 10^{-3}\ min^{-1}$. Scavenger experiments indicated the involvement of multiple reactive species in the degradation process, with the strongest inhibition observed in the presence of isopropanol, suggesting an important contribution from hydroxyl-radical-related processes. The Fe_3O_4-containing nanocomposite also exhibited magnetic responsiveness, which may facilitate catalyst recovery. Overall, the results demonstrate the potential of the PPS/PVA/Fe_3O_4/AgNPs nanocomposite for visible-light-assisted degradation of MO under the investigated laboratory conditions.

K E Y W O R D S

Photocatalysis, Nanocomposites, Methyl Orange, Degradation, Silver Nanoparticles (AgNPs).

Copyright © 2026 The Authors. Published by Payame Noor University.
This work is licensed under a Creative Commons Attribution-NonCommercial 4.0 International license (https://creativecommons.org/licenses/by-nc/4.0/). Non-commercial uses of the work are permitted, provided the original work is properly cited.

1. Introduction

Organic dyes are widely used in textile, food, printing, and other industrial and analytical applications because of their intense coloration, chemical versatility, and commercial importance. However, the discharge of dye-containing effluents into aquatic environments represents an important environmental concern because many synthetic dyes are chemically stable and can persist in water, while their degradation products may also pose ecological risks. The textile industry is a particularly important source of dye-containing wastewater, highlighting the need for more sustainable approaches to textile production and wastewater management [1]. Among synthetic dyes, methyl orange (MO), an anionic azo dye, is frequently used as a model pollutant because of its pronounced visible-light absorption, chemical stability, and resistance to conventional treatment processes. Consequently, the development of efficient, sustainable, and cost-effective approaches for the treatment of dye-contaminated water remains an important environmental challenge [1, 2].

Photocatalytic degradation has emerged as a promising advanced oxidation approach for the removal of organic pollutants from water. Upon irradiation with suitable light, a photocatalyst can generate photogenerated charge carriers that participate in interfacial oxidation–reduction reactions and may produce reactive oxygen species (ROS). These reactive species can attack organic molecules and promote their transformation into smaller products and, under favorable conditions, ultimately toward mineralization. The applicability of photocatalysis to water treatment has been investigated using different semiconductor, polymer-supported, and hybrid photocatalytic systems [2–4]. In addition to pollutant degradation, visible-light-driven photocatalytic systems have also been investigated for sustainable chemical transformations and biomass valorization. For example, a Fe_3O_4@g-CN-DA-SO_3H nanohybrid was recently investigated for the visible-light-assisted conversion of fructose to value-added furan derivatives, demonstrating the broader applicability of light-driven catalytic systems beyond pollutant removal [5]. Recent studies have also reported visible-light- or sunlight-assisted photocatalytic treatment of pharmaceutical pollutants such as azithromycin, sertraline, and clopidogrel [6–8]. Similarly, sunlight-driven nanocatalytic systems based on Pd/$ZnMn_2O_4$/chitosan and magnetic Pd/$NiFe_2O_4$/chitosan have been investigated for the degradation of Congo red dye [9, 10]. These recent studies highlight the continuing development of hybrid and magnetic photocatalysts for the treatment of chemically diverse organic compounds.

Despite these advantages, the practical performance of photocatalysts can be limited by several factors, including insufficient visible-light utilization, rapid electron–hole recombination, limited accessibility of active sites, inadequate interaction between the catalyst and pollutant, and difficulties associated with catalyst separation and reuse. Various strategies have therefore been developed to improve photocatalytic performance, including semiconductor coupling, incorporation of metallic nanoparticles, construction of heterostructures, and immobilization or dispersion of active inorganic phases within polymeric or other functional supports [3, 4]. In particular, coupling photocatalytically active inorganic components with functional materials can modify interfacial charge-transfer pathways and improve the utilization of photogenerated charge carriers. The incorporation of noble-metal

nanoparticles has also been investigated because of their favorable electronic and optical properties [11, 12]. However, the effectiveness of these approaches depends strongly on the composition, morphology, interfacial structure, and preparation method of the resulting hybrid material.

Polyphenylene sulfide (PPS) is a high-performance engineering polymer characterized by high chemical resistance, thermal stability, and mechanical rigidity. These properties make PPS an attractive candidate as a durable polymeric matrix or structural support for functional composite materials. Previous research has reviewed the preparation, properties, applications, processing, and recycling of PPS-based materials, highlighting the versatility and chemical robustness of this polymer [13]. In addition to its role as a structural polymer, PPS itself has also been investigated as a metal-free photocatalytic material, demonstrating that its role in photocatalytic systems may extend beyond that of a passive support [14]. Furthermore, PPS-based porous and composite materials have been explored for visible-light photocatalysis [15]. These findings provide a basis for considering PPS as both a chemically resistant polymeric component and a potentially functional constituent of photocatalytic hybrid materials.

Polyvinyl alcohol (PVA) is another useful polymeric component for the preparation of polymer–inorganic hybrid materials because of its hydrophilicity, film-forming capability, and abundant hydroxyl groups. The hydroxyl groups of PVA can interact with inorganic particles and may improve their dispersion and interfacial compatibility within a composite. Such interactions can influence the accessibility of inorganic active phases to the aqueous reaction medium and may contribute to the structural integrity of the hybrid material. Polymer-based nanocomposite systems have therefore been investigated for water-treatment and photocatalytic applications [4]. The combination of PPS with PVA provides an opportunity to integrate the chemical and mechanical stability of PPS with the hydrophilic and functional characteristics of PVA.

Among magnetic inorganic materials, Fe_3O_4 nanoparticles are particularly attractive for the development of recoverable photocatalysts because their magnetic response enables separation of the catalyst from aqueous media using an external magnetic field. Fe_3O_4 can also participate in interfacial interactions with other components of a composite and may influence surface adsorption and charge-transfer processes. Magnetic photocatalytic nanocomposites have consequently received considerable attention for water treatment because they can combine catalytic activity with improved catalyst recovery. The incorporation of Fe_3O_4 into polymeric matrices can also modify the surface and textural properties of the resulting composite.

Silver nanoparticles (AgNPs) have attracted considerable attention in functional nanomaterials because of their electrical, optical, and catalytic properties. In particular, their surface plasmon resonance (SPR) can contribute to enhanced interaction with visible light, while their electronic properties may facilitate interfacial charge-transfer processes in appropriately designed photocatalytic systems [11]. The size-dependent electronic properties of Ag nanoparticles can also influence their interfacial behavior and performance [12]. Consequently, incorporation of AgNPs into a photocatalytic hybrid material may provide an additional pathway for improving light utilization and facilitating interfacial electron-transfer processes. Nevertheless, these effects depend strongly on nanoparticle size, dispersion, interfacial contact, and the electronic structure of the overall composite.

A particularly relevant strategy is therefore the combination of PPS, PVA, Fe_3O_4, and AgNPs within a single hybrid nanocomposite. Previous work on PPS/PVA/Fe_3O_4/AgNPs has demonstrated the feasibility of constructing a ternary polymer–inorganic composite for visible-light photocatalytic degradation of methylene blue [16]. Building on this concept, the incorporation of AgNPs provides an opportunity to further modify the optical and interfacial properties of the ternary system. In the proposed PPS/PVA/Fe_3O_4/AgNPs nanocomposite, PPS can provide a chemically resistant structural framework, while PVA can contribute hydrophilic functionality and facilitate interactions between the polymeric and inorganic phases. Fe_3O_4 can provide magnetic responsiveness and facilitate catalyst recovery, whereas AgNPs may contribute to visible-light interaction and interfacial electron-transfer processes. The overall photocatalytic behavior is therefore expected to depend on the dispersion, distribution, and interactions among all four components.

In the present study, a PPS/ PVA/ Fe_3O_4/AgNPs nanocomposite was prepared and systematically investigated for the visible-light-driven degradation of methyl orange (MO) in aqueous solution. The synthesized materials were characterized using complementary structural, chemical, morphological, textural, and magnetic techniques to establish the physicochemical properties of the composite. The photocatalytic degradation of MO was evaluated under visible-light irradiation, and the effects of the individual components and their combination were investigated. The apparent photocatalytic kinetics, possible contributions of reactive species, and reusability of the nanocomposite were also examined. The results were used to evaluate how incorporation of Fe_3O_4 and AgNPs into the PPS/PVA matrix influences the physicochemical properties and photocatalytic performance of the resulting hybrid material.

2. Experimental

2.1. Materials

In this study, polyphenylene sulfide (PPS) was provided in the form of white granules (Mn = 21,000, Mw = 48,000, density = 1.82 g cm^{-3}, melting point = 285 °C, and glass transition temperature = 85 °C) from MOCOM Compounds GmbH & Co. KG, Germany, as a commercial product. Analytical-grade reagents were used throughout the experiments. They included ferric chloride ($FeCl_3 \cdot 6H_2O$), methyl orange (MO), ferrous chloride ($FeCl_2 \cdot 4H_2O$), sodium citrate, silver nitrate ($AgNO_3$), sodium borohydride ($NaBH_4$), sodium hydroxide (NaOH), ammonia (NH_4OH), and polyvinyl alcohol (PVA), all of which were obtained from Merck, Germany. Deionized water, prepared in the laboratory, was used throughout the experimental procedures.

2.2. Synthesis of silver nanoparticles

The preparation of silver nanoparticles was carried out by mixing equal volumes of 20 mL each of 0.05 M sodium citrate and 0.05 M silver nitrate ($AgNO_3$) solutions with 160 mL of ultrapure water in a controlled environment, whereby the temperature was set between 6 °C and 10 °C. The mixture was then stirred forcefully at a rate of 3000 RPM for three minutes. Afterward, 20 mL of 0.05 M sodium borohydride was slowly added to the solution. To ensure optimal nanoparticle formation, the pH of the solution was accurately set to 10 with 1.25 M sodium hydroxide. The silver nanoparticles were subsequently carefully preserved in dark and chilled glass jars at 4 °C for further analysis and experimental uses.

2.3. Synthesis of nanocomposites

The PPS granules were first dry-ball-milled using steel balls for 24 h to obtain finely powdered PPS. Subsequently, 0.1 g of the powdered PPS was dispersed in 50 mL of deionized water and ultrasonicated for 60 min. Separately, 0.2 g of PVA was dissolved in 50 mL of deionized water at 90 °C under magnetic stirring for 60 min. The PPS suspension was then added to the PVA solution, and the mixture was stirred at 90 °C for an additional 60 min to obtain a homogeneous suspension.

Next, 0.475 g of $FeCl_2 \cdot 4H_2O$ and 0.951 g of $FeCl_3 \cdot 6H_2O$ were dissolved in 50 mL of deionized water and added to the suspension. The mixture was stirred at 90 °C for 60 min. A 25% ammonia solution was then added to adjust the pH to approximately 11, resulting in the formation of a black precipitate. Stirring was continued for a further 30 min.

Afterward, 0.1 g of the previously prepared AgNPs, dispersed in 20 mL of deionized water, was added to the reaction mixture at approximately 70 °C. The mixture was stirred for another 30 min and then allowed to cool naturally to room temperature. The precipitate was collected using an external magnet and washed several times with deionized water until the washings reached neutral pH. Finally, the product was dried at 40 °C for 24 h, ground, and stored for subsequent experiments.

The PPS/Fe_3O_4, PVA/Fe_3O_4, PPS/PVA/Fe_3O_4, and bare Fe_3O_4 samples were prepared using the same co-precipitation procedure, with the relevant polymer components omitted as appropriate. The preparation procedure is illustrated schematically in Fig. 1.

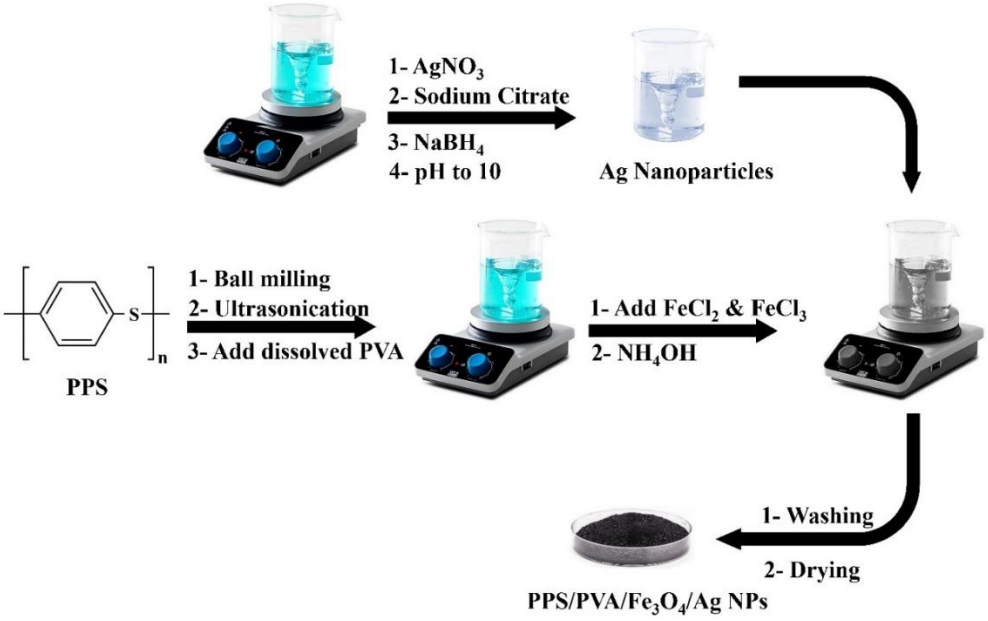

Fig. 1 Schematic pattern for synthesizing the PPS/PVA/ Fe_3O_4/AgNPs nanocomposite.

2.4. Characterization

The prepared materials were characterized using various analytical techniques to investigate their structural, chemical, morphological, optical, magnetic, and colloidal properties. X-ray diffraction (XRD) patterns were recorded using a PHILIPS X'PERT PRO X-ray diffractometer with Cu Kα radiation (λ = 1.54 Å) over a 2θ range of 10–80°. Fourier-transform infrared (FT-IR) spectra were

obtained using a SHIMADZU IRPrestige-21 spectrometer in the range of 4000–500 cm^{-1}. The morphology and surface features of the prepared samples were examined using a field-emission scanning electron microscope (FESEM, MIRA III VEGA-TESCANXMU). Dynamic light scattering (DLS) measurements were performed using a SZ-100 HORIBA Scientific instrument at a scattering angle of 90° to investigate the particle-size distribution of the samples (International Organization for Standardization) [17]. UV–Vis absorption measurements were carried out using a GBC CINTRA 20 double-beam spectrophotometer. The magnetic properties of the prepared samples were investigated using an MDKB vibrating sample magnetometer (VSM).

2.5. Photocatalytic Activity

The photocatalytic activity of the prepared samples was evaluated through the degradation of methyl orange (MO) in aqueous solution under visible-light irradiation at room temperature. The experiments were conducted using a custom-made wooden photoreactor equipped with a 50 W LED lamp as the visible-light source. A compact fan was used to provide continuous airflow during irradiation.

For each experiment, 0.10 g of catalyst was added to 100 mL of an aqueous MO solution with an initial concentration of 10 mg L^{-1} at approximately neutral pH. Before irradiation, the suspension was magnetically stirred in the dark for 60 min to establish adsorption–desorption equilibrium between the catalyst surface and MO molecules. The suspension was then exposed to visible light for 120 min. Aliquots were collected at 15-min intervals during irradiation, and the catalyst particles were separated from the suspension before analysis [18].

The concentration of MO was monitored by measuring the absorbance of the supernatant at 503 nm using a UV–Vis spectrophotometer. The degradation efficiency (η) was calculated according to Eq. (1):

$$\eta\ (\%) = [(A_0 - A_t)/A_0] \times 100$$

where A_0 is the initial absorbance of the MO solution after establishing the initial experimental conditions, and A_t is the absorbance at irradiation time t [18].

All photocatalytic experiments were performed in triplicate, and the mean values were used for data analysis.

The photocatalytic degradation kinetics were evaluated using the apparent pseudo-first-order kinetic model, which can be expressed as:

$$\ln(C_0/C_t) = k_{app}t$$

where C_0 and C_t represent the MO concentrations at the initial time and at irradiation time t, respectively, and k_{app} is the apparent pseudo-first-order rate constant. The value of k_{app} was obtained from the slope of the linear plot of $\ln(C_0/C_t)$ versus irradiation time [18].

2.6. Reactive Species Trapping Experiments

Scavenger experiments were performed to investigate the possible involvement of reactive species in the photocatalytic degradation of MO. Ascorbic acid (AA), isopropyl alcohol (IPA), and potassium iodide (KI) were used as scavengers for selected reactive species at a concentration of 0.01 M [19, 20].

Before visible-light irradiation, the corresponding scavenger was added to the MO suspension containing the photocatalyst. The photocatalytic degradation experiments were then performed under the same conditions described in Section 2.5. The degradation efficiency obtained in the presence of each scavenger was compared with that obtained in the absence of a scavenger [19, 20].

A decrease in MO degradation efficiency following the addition of a particular scavenger was interpreted as evidence for the possible involvement of the corresponding reactive species in the photocatalytic process. These experiments were therefore used to obtain mechanistic information regarding the reactive species participating in the degradation of MO [19, 20].

3.1. Structural Analysis

The XRD patterns presented in Fig. 2 provide information on the crystalline structures and phase composition of PPS, PVA, Fe_3O_4, AgNPs, and the PPS/PVA/Fe_3O_4/AgNPs nanocomposite. The diffraction pattern of PPS exhibits a relatively sharp reflection at 2θ = 18.46°, together with a broad diffraction feature centered at approximately 21.36°, a shoulder near 23.84°, and a weaker reflection at 42.34°. These features are consistent with the semi-crystalline nature of PPS and the coexistence of ordered and less-ordered domains in the polymer matrix [14, 16].

The XRD pattern of Fe_3O_4 shows characteristic reflections at 2θ = 31.24°, 36.46°, 44.50°, 58.12°, and 64.68°, which have been assigned to the (220), (311), (400), (511), and (440) planes, respectively, of the cubic spinel structure of magnetite [16]. The absence of additional distinct crystalline reflections in the Fe_3O_4 pattern suggests that no other crystalline phase was detected within the detection capability of the XRD measurement.

The synthesized AgNPs exhibit diffraction peaks at 2θ = 38.41°, 46.73°, 66.27°, and 77.89°, which are consistent with the characteristic reflections of face-centered cubic (fcc) metallic silver [21]. In the PPS/PVA/Fe_3O_4/AgNPs nanocomposite, the characteristic reflections of the inorganic components are observed together with the polymeric background, although some reflections become less pronounced because of peak overlap, reduced phase content, and the polymer matrix [16].

The Fe_3O_4-related reflections in the nanocomposite show slight shifts toward lower 2θ values compared with those of the pristine Fe_3O_4 sample. Such shifts may be associated with changes in the local structural environment of Fe_3O_4 within the composite matrix and possible interfacial interactions with the polymeric components. However, the XRD results alone do not establish the precise nature of these interactions.

The crystallite sizes were estimated using the Debye–Scherrer equation:

$$D = K\lambda/(\beta \cos \theta)$$

where D is the mean crystallite size, K is the shape factor (0.94), λ is the Cu Kα wavelength (0.15418 nm), β is the full width at half maximum (FWHM) of the selected diffraction peak expressed in radians, and θ is the corresponding Bragg angle. The calculated crystallite sizes are summarized in Table 1. The values were 25.51, 11.93, 8.71, 27.57, and 17.80 nm for PPS, PVA, Fe_3O_4, AgNPs, and the PPS/PVA/ Fe_3O_4/AgNPs nanocomposite, respectively [22].

The calculated crystallite size of the nanocomposite is lower than that of pristine PPS, indicating a reduction in the average size of coherent crystalline domains after incorporation of the additional components. This change may be associated with disruption of the ordered PPS domains during the formation of the multicomponent composite. Nevertheless, the crystallite-size data alone should not be interpreted as a quantitative measure of the degree of crystallinity [22].

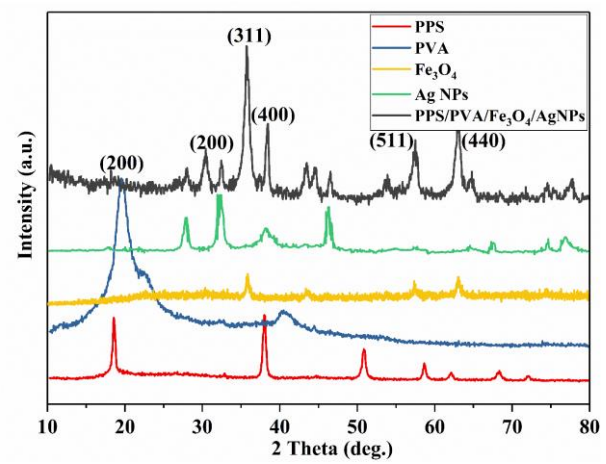

Fig. 2 XRD spectra of PPS, PVA, Fe_3O_4, AgNPs, and the PPS/PVA/Fe_3O_4/AgNPs composite.

Table 1: lists the crystallite sizes of the samples, as estimated from the XRD peaks.

Sample	Crystallite size (nm)
PPS	25.51
PVA	11.93
Fe_3O_4	8.71
AgNPs	27.57
PPS/PVA/Fe_3O_4/AgNPs	17.80

3.2. Chemical analysis

The FT-IR spectra of PPS, PVA, Fe_3O_4, and the PPS/PVA/Fe_3O_4/AgNPs nanocomposite are presented in Fig. 3.

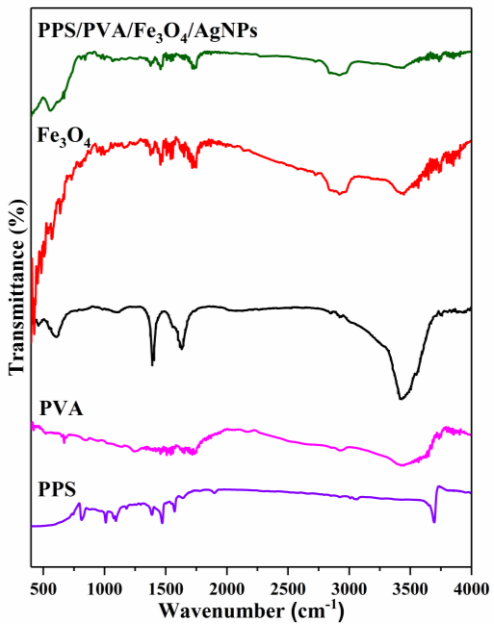

Fig. 3 FT-IR spectrum of PPS, PVA, Fe_3O_4, and the PPS/PVA/Fe_3O_4/AgNPs composite.

The PPS spectrum shows characteristic aromatic C–H stretching vibrations in the 3000–3100 cm^{-1} region and C=C/C–C skeletal vibrations in the 1400–1600 cm^{-1} range, consistent with the poly(phenylene sulfide) structure. The PVA spectrum exhibits a broad absorption band around 3465 cm^{-1}, mainly associated with O–H stretching vibrations. Additional bands in the 1400–1450 and 1300–1400 cm^{-1} regions are attributed to vibrations of the PVA polymer structure, while the band near 1079 cm^{-1} is associated with C–O stretching vibrations. The absorption band of Fe_3O_4 around 563 cm^{-1} is consistent with Fe–O vibrations in the iron oxide structure. In the PPS/PVA/Fe_3O_4/AgNPs nanocomposite, characteristic spectral features of the constituent materials are retained, although changes in band intensity and position are observed. These changes may reflect modifications in the local chemical environments of the functional groups following incorporation of the inorganic components into the polymer matrix [16]. A broad absorption band near 3492 cm^{-1} can be associated with O–H stretching vibrations arising from hydroxyl groups and/or adsorbed moisture. Overall, the FT-IR results are consistent with the presence of the constituent materials and indicate changes in their local chemical environments. However, FT-IR evidence alone is insufficient to establish the formation of specific new chemical bonds, such as Fe–O–C, or to demonstrate oxidative conversion or crosslinking of the PPS structure.

3.3. EDX analysis

Energy-dispersive X-ray (EDX) spectroscopy and elemental mapping were employed to investigate the elemental composition and spatial distribution of the constituent elements in PPS and the PPS/PVA/Fe_3O_4/AgNPs

nanocomposite. The corresponding elemental maps and EDX spectra are presented in Fig. 4.

The elemental mapping images of PPS and the PPS/PVA/Fe_3O_4/AgNPs nanocomposite are shown in Fig. 4a and e, respectively. The elemental maps of the nanocomposite illustrate the spatial distribution of carbon (C), oxygen (O), sulfur (S), iron (Fe), and silver (Ag) within the analyzed region. The corresponding EDX spectra shown in Fig. 4b–d and f–j provides additional evidence for the detection of these elements in the analyzed samples.

As summarized in Table 2, the elemental composition of PPS is dominated by carbon and sulfur, with C and S contents of 59.15 and 29.20 wt%, respectively. In comparison, the PPS/ PVA/ Fe_3O_4/ AgNPs nanocomposite contains 15.64 wt% C, 37.46 wt% O, 6.75 wt% S, 32.64 wt% Fe, and 6.83 wt% Ag. The lower relative C and S contents and higher O content in the analyzed composite region are consistent with the incorporation of PVA and the inorganic components into the PPS-based material. The detected Fe and Ag signals further support the presence of Fe- and Ag-containing components in the analyzed region.

Elemental mapping provides information about the spatial distribution of detected elements within the analyzed area. However, EDX mapping is area-dependent and should not be interpreted as a direct quantitative determination of the bulk composition. Accordingly, the weight percentages reported in Table 2 should be regarded as semi-quantitative values, whose accuracy may depend on the analyzed region, sample morphology, preparation, and measurement conditions [23].

EDX identifies elemental composition but does not, by itself, establish the chemical bonding state or crystalline phase of the detected elements. Therefore, the detection of Fe and Ag by EDX is complementary to the XRD results, which provide information about the crystalline phases present in the nanocomposite.

Overall, the EDX spectra and elemental mapping results support the presence of the principal elements associated with the PPS/PVA/Fe_3O_4/AgNPs nanocomposite and are consistent with the incorporation of the inorganic components into the polymer-based matrix.

Table 2: provides the fundamental composition of the PPS and PPS/PVA/ Fe_3O_4/AgNPs samples, as determined by EDX analysis.

Sample	The weight percentage of elements %				
	C	O	S	Fe	Ag
PPS	59.15	8.11	29.2		
PPS/PVA/Fe_3O_4/AgNPs	15.64	37.46	6.75	32.64	6.83

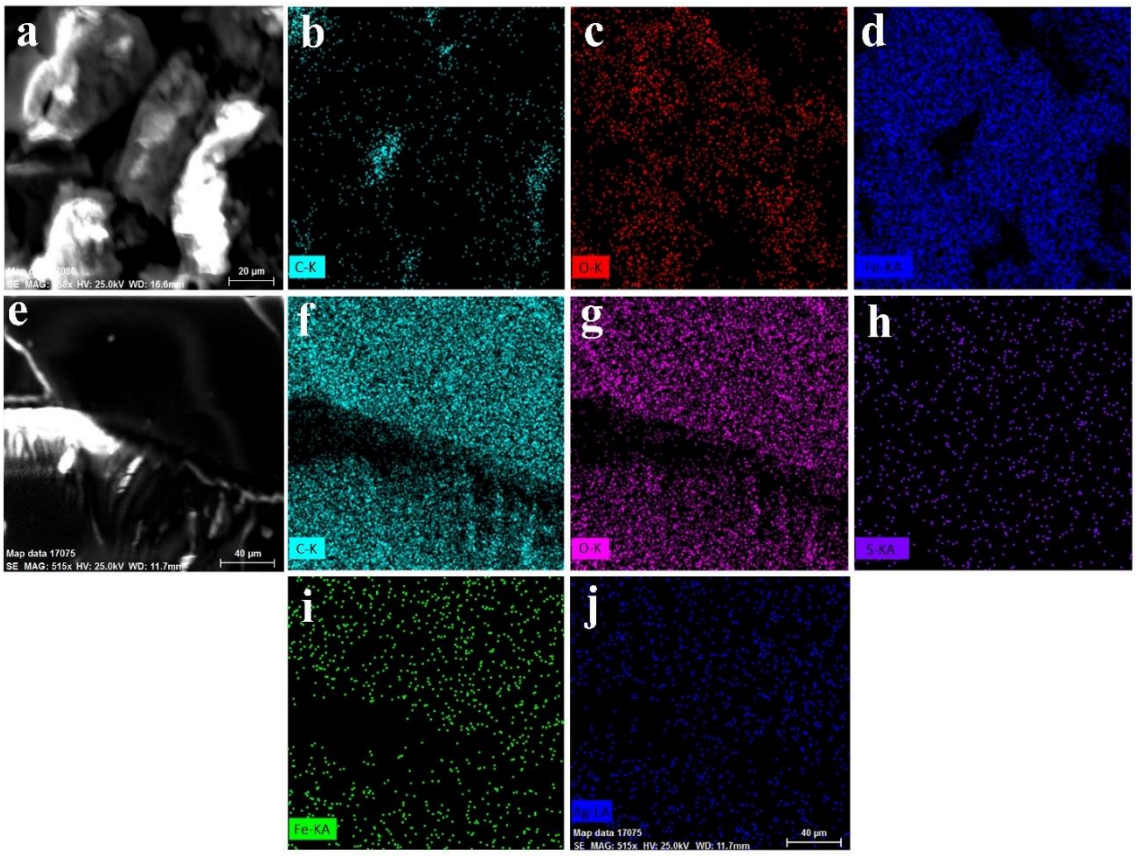

Fig.4 (a) Elemental mapping image of PPS and (b-d) corresponding EDX spectra; (e) Elemental mapping image of the PPS/PVA/Fe_3O_4/AgNPs nanocomposite and (f-j) corresponding EDX spectra.

3.4. Magnetic Properties

The magnetic properties of the prepared materials were investigated by vibrating sample magnetometry (VSM), and the corresponding magnetization curves are presented in Fig. 5. PPS and PVA exhibit no significant magnetic response, whereas the Fe_3O_4 nanoparticles show a saturation magnetization of 51.5 emu g^{-1} at an applied magnetic field of 10,000 Oe. After incorporation of Fe_3O_4 into the PPS/PVA/Fe_3O_4/AgNPs nanocomposite, the saturation magnetization decreases to 23.53 emu g^{-1}. This decrease is consistent with a dilution effect arising from the presence of the non-magnetic polymeric components and AgNPs, which contribute to the total sample mass without providing a comparable magnetic response [24].

Despite its lower saturation magnetization compared with pristine Fe_3O_4, the nanocomposite retains a measurable magnetic response to an external magnetic field. This response may facilitate magnetic separation of the material from aqueous media and could be advantageous for catalyst recovery and potential reuse. The practical effectiveness of magnetic recovery, however, should be evaluated based on direct separation or recovery experiments.

The VSM results therefore support the presence of a magnetically responsive Fe_3O_4-containing component in the PPS/PVA/Fe_3O_4/AgNPs nanocomposite. The combination of photocatalytic activity and

magnetic responsiveness may be beneficial for photocatalytic treatment processes by providing a potential route for separating the catalyst from the treated suspension using an external magnetic field [25].

Although the magnetization curve exhibits an S-shaped profile, the assignment of the magnetic behavior specifically as superparamagnetic requires consideration of the coercivity and remanent magnetization obtained from the hysteresis loop. Therefore, the present results are interpreted primarily in terms of saturation magnetization and magnetic responsiveness rather than as definitive evidence of superparamagnetism.

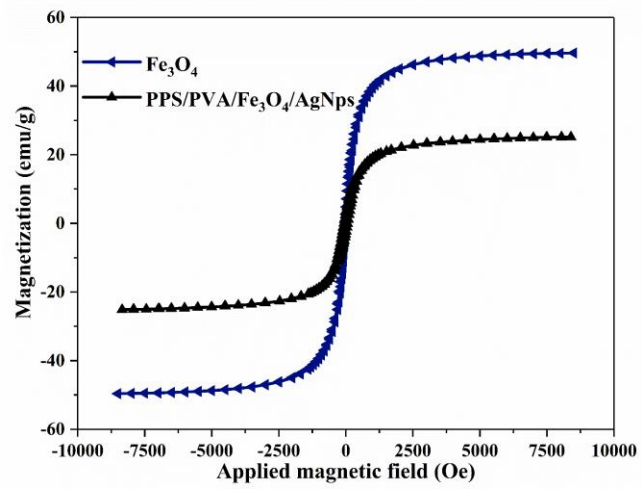

Fig. 5 Magnetization plots versus applied magnetic field (VSM) for Fe_3O_4 and the PPS/PVA/Fe_3O_4/AgNPs composite.

3.5. BET Surface Area and BJH Pore Size Distribution

The nitrogen adsorption–desorption isotherms of pure PPS and the PPS/PVA/Fe_3O_4/AgNPs nanocomposite are presented in Fig. 6a. The isotherm of PPS exhibits features consistent with a Type IV isotherm accompanied by an H3-type hysteresis loop. Type IV isotherms are generally associated with mesoporous materials and pore filling through capillary condensation, whereas H3-type hysteresis is commonly observed for aggregates of plate-like particles and is associated with slit-shaped pore structures [26].

Compared with pure PPS, the PPS/PVA/Fe_3O_4/AgNPs nanocomposite exhibits a pronounced increase in nitrogen adsorption over the measured relative-pressure range. As summarized in Table 3, the BET specific surface area increases from 1.52 $m^2\ g^{-1}$ for pure PPS to 26.68 $m^2\ g^{-1}$ for the nanocomposite. This increase indicates that the composite has a substantially larger surface area accessible to nitrogen under the measurement conditions. The higher accessible surface area may provide additional sites for adsorption and surface interactions with methyl orange molecules and may therefore contribute to the adsorption–photocatalysis performance of the nanocomposite.

Further information on the textural properties was obtained from Barrett–Joyner–Halenda (BJH) pore-size distribution analysis, as shown in Fig. 6b and summarized in Table 3. Compared with pure PPS, the nanocomposite exhibits changes in both average pore diameter and total pore volume. The decrease in average pore diameter, together with the increase in total pore volume, indicates a modification of the measured pore characteristics following incorporation of PVA, Fe_3O_4, and AgNPs into the PPS matrix. These changes may be associated with the distribution and aggregation of the inorganic nanoparticles and polymeric components, which can alter the accessible pore structure. However, the specific structural origin of these changes cannot be established from BET and BJH results alone.

Overall, the BET and BJH results indicate a substantial modification of the textural properties of PPS following incorporation of PVA, Fe_3O_4, and AgNPs. The higher specific surface area may provide more accessible sites for interaction with MO molecules, potentially

contributing to the adsorption–photocatalysis performance. However, this interpretation should be assessed in conjunction with the photocatalytic results. Nevertheless, BET and BJH analyses alone do not establish the photocatalytic mechanism or demonstrate enhanced charge separation; these aspects should be assessed in conjunction with the photocatalytic and other characterization results.

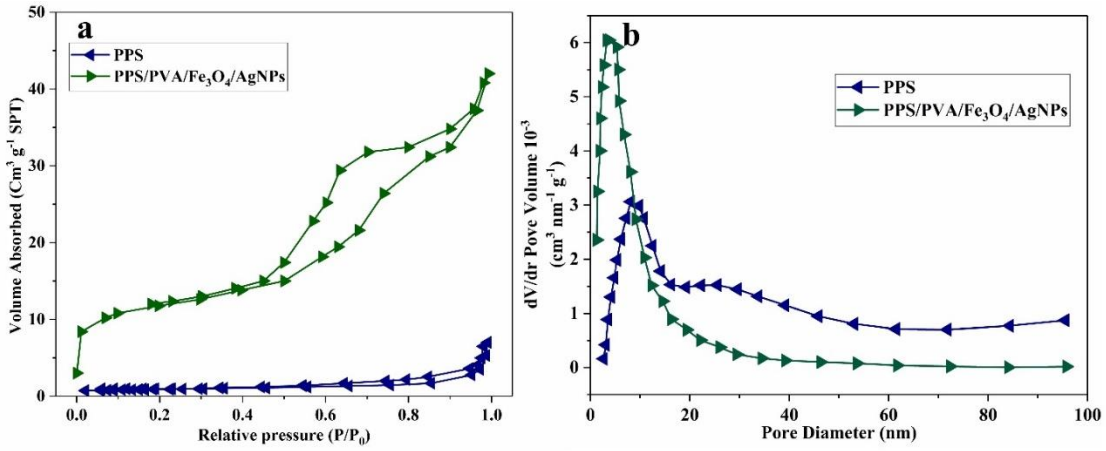

Fig. 6 (a) BET isotherms and (b) pore size distribution of PPS and the PPS/PVA/Fe_3O_4/AgNPs nanocomposite.

Table 3: Textural properties of PPS and the PPS/PVA/Fe_3O_4/AgNPs samples.

Sample	BET surface area ($m^2 g^{-1}$)	Total pore volume ($cm^3 g^{-1}$)	Mean pore diameter (nm)
PPS	1.52	0.02	29.30
PPS/PVA/Fe_3O_4/AgNPs	26.68	0.08	12.12

3.6. Morphological Studies

Field-emission scanning electron microscopy (FESEM) was employed to examine the surface morphology of pure polyphenylene sulfide (PPS) and the PPS/PVA/Fe_3O_4/AgNPs nanocomposite, as shown in Fig. 7. The FESEM images of PPS reveal an irregular and relatively planar surface morphology with a heterogeneous texture. In comparison, the FESEM images of the PPS/PVA/Fe_3O_4/AgNPs nanocomposite (Fig. 7d–f) show noticeable changes in surface morphology following the incorporation of PVA, Fe_3O_4, and AgNPs. The composite surface appears more heterogeneous, with dispersed features and some regions of aggregation. These morphological changes are consistent with modification of the PPS surface following incorporation of the polymeric and inorganic components.

The FESEM images were used exclusively for qualitative evaluation of surface morphology and aggregation features. No quantitative particle-size analysis (including software-based image analysis, particle counting, or statistical calculation of an average particle size) was performed on the FESEM images. Accordingly, the observed morphological features are discussed qualitatively and are not used to derive numerical particle-size values.

The particle-size characteristics of PPS and the PPS/PVA/Fe_3O_4/AgNPs nanocomposite were further investigated by dynamic light scattering (DLS), as shown in Fig. 8. Unlike FESEM, which probes the morphology of dried

samples under high vacuum, DLS determines the hydrodynamic diameter of particles dispersed in a liquid medium [17]. The measured hydrodynamic diameters were approximately 272 nm for PPS and 263 nm for the PPS/PVA/Fe_3O_4/AgNPs nanocomposite. These DLS values represent hydrodynamic diameters in suspension and should not be interpreted as direct geometric particle diameters of the dried solid, as they are influenced by factors such as surface structure, solvation/hydration layers, ionic strength, and the aggregation state of particles in the dispersing medium [17].

The DLS measurements therefore provide complementary information to the FESEM observations. While FESEM reveals qualitative information on the surface morphology of dried samples, DLS provides quantitative information on the hydrodynamic size of particles in dispersion. The slight difference between the measured DLS values reflects a modest difference in the hydrodynamic size characteristics of the two samples.

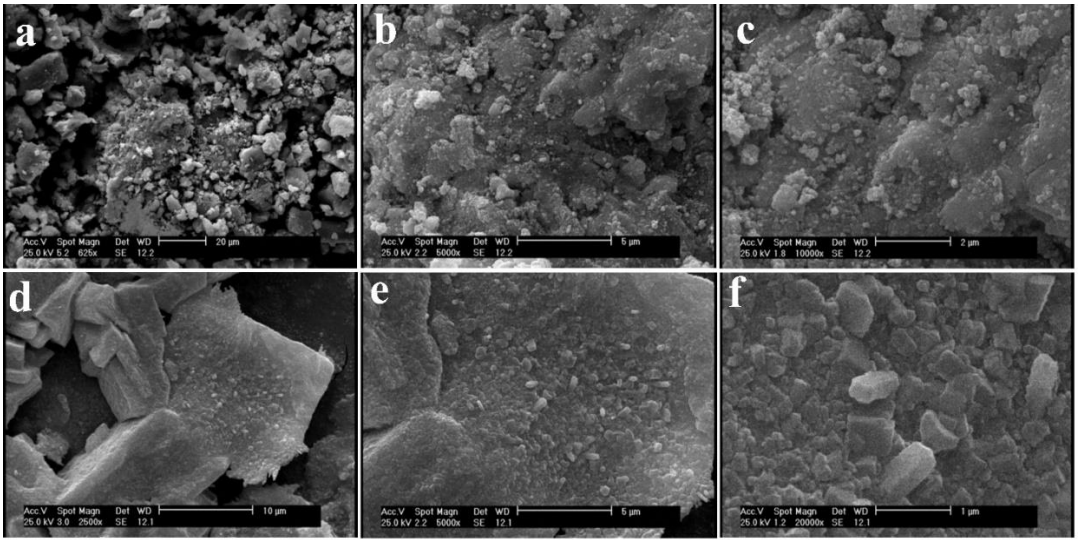

Fig.7 FESEM images of (a-c) PPS and (d-f) the PPS/PVA/Fe_3O_4/ AgNPs nanocomposite.

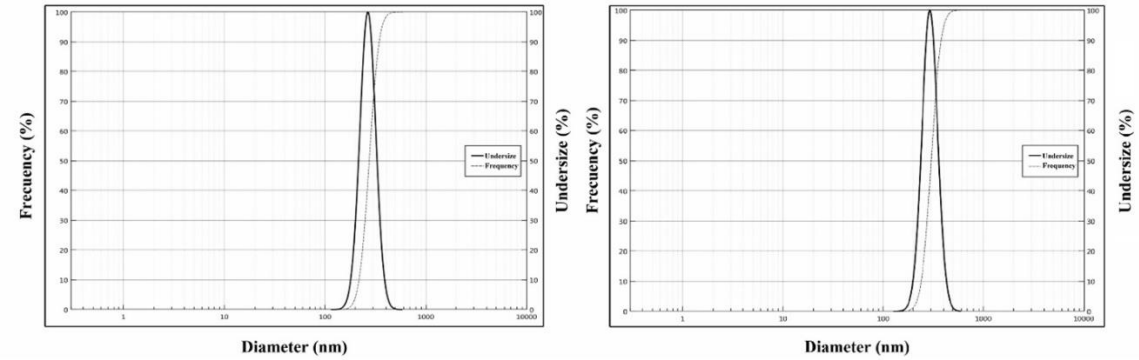

Fig. 8 DLS results for (a) PPS and (b) the PPS/PVA/Fe_3O_4/AgNPs nanocomposite.

3.7. Photocatalytic Activity

The photocatalytic activities of the synthesized samples were evaluated by monitoring the degradation of methyl orange (MO) under visible-light irradiation at neutral pH. The changes in the UV–Vis absorption spectra of MO as a function of irradiation time are presented in Fig. 9. The decrease in the characteristic absorption band of MO at 503 nm was used to monitor the degradation process.

The degradation efficiency was calculated from the change in absorbance according to Eq. (1).

As shown in Fig. 9a, pure PPS exhibited a degradation efficiency of approximately 39% after 120 min of visible-light irradiation. This activity may be associated with the surface properties of PPS and its interaction with MO molecules. PVA exhibited a slightly lower degradation efficiency of approximately 38% under the same conditions (Fig. 9b). Fe_3O_4 exhibited lower degradation performance than the polymeric components (Fig. 9c). This behavior may be related to differences in surface properties, dispersion state, and accessibility of the catalyst surface under the applied experimental conditions.

The incorporation of PVA and Fe_3O_4 into PPS considerably improved the degradation performance. As shown in Fig. 9d, the PPS/PVA/Fe_3O_4 nanocomposite achieved approximately 62% MO degradation after 120 min. The enhanced performance compared with the individual components may be associated with the combined contribution of the polymeric and inorganic phases and the resulting changes in the surface and interfacial properties of the nanocomposite. However, the individual contribution of each component cannot be established solely from the degradation results and should therefore be interpreted together with the other characterization and mechanistic data.

A further improvement was observed after incorporation of AgNPs. The PPS/PVA/Fe_3O_4/AgNPs nanocomposite exhibited approximately 91% MO degradation after 120 min of visible-light irradiation (Fig. 9e). The enhanced photocatalytic performance may be associated with the contribution of AgNPs to visible-light absorption and interfacial charge-transfer processes. In addition, the presence of Fe_3O_4 and AgNPs may modify the surface and interfacial properties of the polymeric matrix and thereby influence the interaction of MO with the catalyst surface. These interpretations are considered together with the other characterization and mechanistic results.

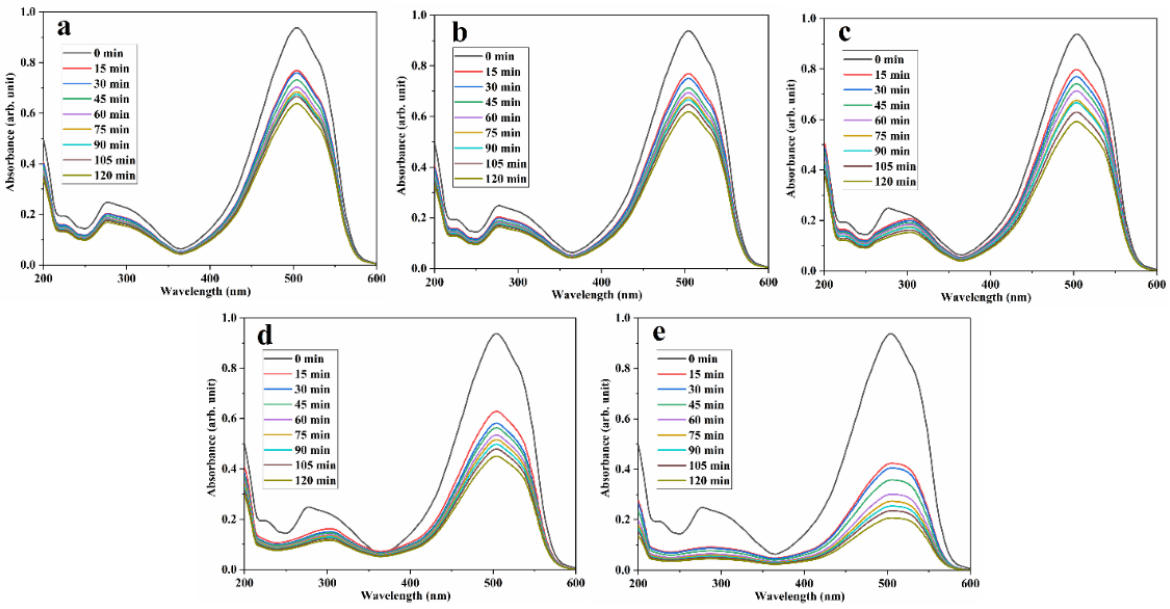

Fig. 9 Time-dependent UV-Vis absorption spectra for the degradation of MO solution by PPS, PVA, Fe_3O_4, AgNPs, PPS/PVA/Fe_3O_4, and the PPS/PVA/Fe_3O_4/AgNPs.

The degradation behavior of MO over time for PPS, PVA, Fe_3O_4, AgNPs, PPS/PVA/Fe_3O_4, and PPS/PVA/Fe_3O_4/AgNPs is presented in Fig. 10a. The experiments performed under dark conditions provide information on the adsorption and equilibration of MO on the catalyst surface before visible-light irradiation. Following the dark equilibration period, the subsequent decrease in MO concentration under irradiation reflects the combined effects of adsorption and photocatalytic transformation. Among the investigated samples, the PPS/PVA/Fe_3O_4/AgNPs nanocomposite exhibited the highest overall MO removal under the applied experimental conditions.

To compare the apparent degradation kinetics, the experimental data obtained during the irradiation stage were analyzed using a pseudo-first-order kinetic model according to Eq. (2) [18, 27].

$$\ln(C_0/C_t) = k_{app}t$$

where C_0 represents the MO concentration at the beginning of the irradiation stage, after the dark equilibration period, and C_t represents the MO concentration at irradiation time t. The parameter k_{app} is the apparent pseudo-first-order rate constant (min^{-1}). The corresponding linear plots are presented in Fig. 10b. The calculated apparent rate constants were 23×10^{-4}, 27×10^{-4}, 25×10^{-4}, 32×10^{-4}, 86×10^{-4}, and 9.1×10^{-3} min^{-1} for PPS, PVA, Fe_3O_4, AgNPs, PPS/PVA/Fe_3O_4, and PPS/PVA/Fe_3O_4/AgNPs, respectively. As shown in Fig. 10c, the PPS/PVA/Fe_3O_4/AgNPs nanocomposite exhibits the highest apparent rate constant among the investigated samples, indicating the highest apparent MO degradation rate under the applied experimental conditions.

It is important to distinguish MO decolorization or degradation from complete mineralization. A decrease in the MO concentration or absorbance at 503 nm indicates the removal or transformation of the chromophore species but does not, by itself, demonstrate complete conversion of the organic molecules into CO_2, H_2O, and inorganic ions [28]. Therefore, the TOC results presented in Fig. 10d were used to provide additional information regarding changes in the organic carbon content during photocatalytic treatment.

The variation in TOC during irradiation provides additional information on the extent of organic carbon removal or transformation. Accordingly, the TOC results should be discussed independently from the decrease in MO concentration determined by UV–Vis spectroscopy. A decrease in TOC indicates a reduction in the organic carbon remaining in the analyzed solution; however, this decrease may reflect mineralization as well as other removal processes, such as adsorption or separation of catalyst-associated organic species. Therefore, complete mineralization should only be claimed when the TOC results quantitatively support such a conclusion [28]

Overall, the PPS/PVA/Fe_3O_4/AgNPs nanocomposite showed the highest MO degradation efficiency and the highest apparent pseudo-first-order rate constant among the investigated samples under the applied experimental conditions. The photocatalytic results indicate that incorporation of Fe_3O_4 and AgNPs into the PPS/PVA matrix substantially modifies the photocatalytic performance of the resulting nanocomposite.

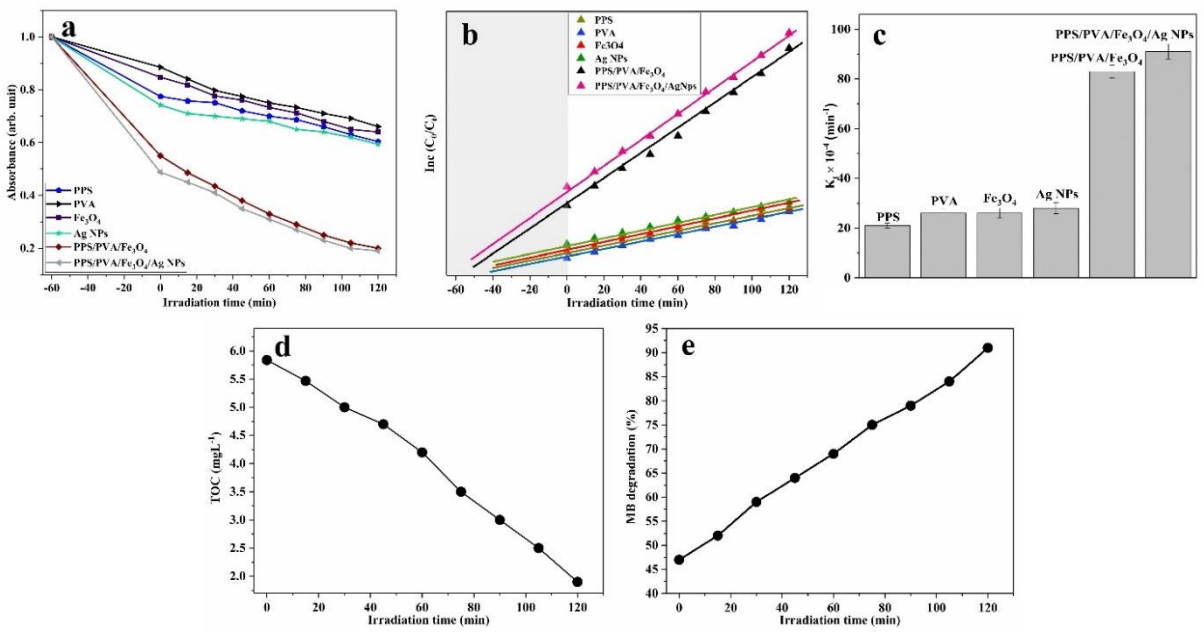

Fig. 10 (a) Photocatalytic activity, (b) $\ln(C_0/C_t)$ plot, (c) apparent pseudo-first-order rate kinetic constant, k_{app} (min^{-1}), and (d) TOC analysis and MO degradation efficiency over time for the PPS/PVA/Fe_3O_4/AgNPs.

3.8. Possible Photocatalytic Mechanism

Based on the photocatalytic results and characterization data, a possible mechanism for the degradation of methyl orange (MO) over the PPS/PVA/Fe_3O_4/AgNPs nanocomposite under visible-light irradiation can be proposed. Upon visible-light irradiation, the components of the nanocomposite may participate in light absorption and interfacial charge-transfer processes. These processes may influence the generation, migration, and recombination of photogenerated charge carriers and thereby affect the availability of reactive species at the catalyst surface.

The photogenerated electrons may participate in the reduction of dissolved oxygen, potentially leading to the formation of reactive oxygen species (ROS), including superoxide radicals ($\bullet O_2^-$). Meanwhile, photogenerated holes may participate in oxidation reactions involving surface-adsorbed water or hydroxyl-containing species, potentially contributing to the formation of hydroxyl radicals (•OH). These reactive species can react with MO molecules and promote their transformation into smaller intermediate products. The involvement of such reactive species in photocatalytic degradation processes is commonly investigated using selective scavenger experiments [20].

The incorporation of Fe_3O_4 and AgNPs into the PPS/PVA matrix may modify the interfacial charge-transfer characteristics of the composite. AgNPs may contribute to visible-light-induced processes and facilitate interfacial electron-transfer interactions, whereas Fe_3O_4 provides an additional inorganic phase with magnetic properties and potential participation in interfacial redox processes. However, the specific charge-transfer pathway among PPS, Fe_3O_4, and AgNPs cannot be conclusively established from the photocatalytic results alone. Therefore, the proposed charge-transfer interactions should be regarded as possible contributions to the enhanced photocatalytic activity rather than as a definitively established pathway.

The increased surface area of the nanocomposite, as demonstrated by the BET

results, may also provide more accessible surface sites for interaction with MO molecules. This may increase the contact between the dye molecules and the catalyst surface and thereby facilitate subsequent photocatalytic reactions [26]. Thus, the enhanced photocatalytic performance may result from the combined effects of surface accessibility, light absorption, interfacial interactions, and the formation and participation of reactive species.

To obtain further insight into the reactive species involved in the photocatalytic degradation process, scavenger experiments were performed using ascorbic acid (AA), isopropanol (IPA), and potassium iodide (KI), each at a concentration of 0.01 M. The experiments were conducted under the same photocatalytic conditions used for the degradation experiments. The apparent degradation rate constant in the absence of a scavenger was 86 × 10^{-4} min^{-1}. In the presence of AA, IPA, and KI, the corresponding rate constants decreased to 44 × 10^{-4}, 21 × 10^{-4}, and 74 × 10^{-4} min^{-1}, respectively, as shown in Fig. 11. Similar scavenger approaches have been used to investigate the participation of $•O_2^-$, •OH, and h^+ in photocatalytic degradation systems [20].

The addition of IPA resulted in the largest decrease in the apparent degradation rate constant, from 86 × 10^{-4} to 21 × 10^{-4} min^{-1}, corresponding to a decrease of approximately 76%. Because IPA is commonly employed as a hydroxyl-radical scavenger, this pronounced inhibition suggests that •OH may make an important contribution to the photocatalytic degradation of MO under the applied experimental conditions [20]

The presence of AA also produced a substantial decrease in the apparent rate constant, from 86 × 10^{-4} to 44 × 10^{-4} min^{-1}, corresponding to a decrease of approximately 49%. Because AA can act as a scavenger of reactive oxygen species, including superoxide-related species, this result suggests that superoxide species may also contribute to MO degradation. However, scavengers are not perfectly selective under all photocatalytic conditions; therefore, the present results should be interpreted as evidence for the involvement of these reactive species rather than as definitive proof of their exclusive participation.

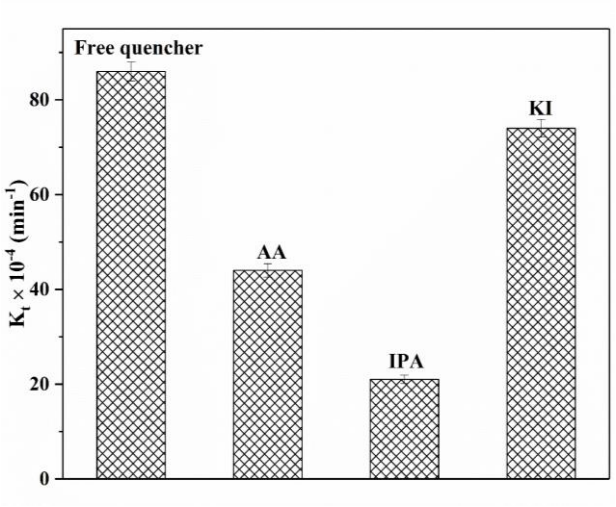

Fig. 11 Results from trapping experiments showing apparent pseudo-first-order rate kinetic constants with three specific quenchers: ascorbic acid (AA), isopropanol (IPA), and potassium iodide (KI), alongside a control.

In comparison, KI caused a relatively smaller decrease in the apparent rate constant, from 86 × 10^{-4} to 74 × 10^{-4} min^{-1}, corresponding to approximately 14%. KI can interact with photogenerated holes and may also affect hydroxyl-radical-related processes [20]. Therefore, the relatively small inhibition observed in the present experiment suggests a less pronounced contribution of the reactive pathways affected by KI under the applied conditions.

Overall, the scavenger experiments indicate that multiple reactive species may participate in MO degradation over the PPS/PVA/Fe_3O_4/AgNPs nanocomposite. The strongest inhibition was

observed in the presence of IPA, suggesting an important contribution from •OH, while the substantial inhibition caused by AA indicates a significant contribution from superoxide-related species. The comparatively smaller effect of KI suggests a less pronounced contribution of the pathways affected by this scavenger. These results support a photocatalytic mechanism involving multiple reactive species rather than a single reaction pathway. Nevertheless, the scavenger experiments alone cannot establish the complete charge-transfer mechanism, and the proposed pathway should therefore be considered a plausible interpretation of the combined characterization, photocatalytic, and scavenger results.

3.9. Reusability Study

The reusability of a photocatalyst is an important factor in evaluating its potential for repeated photocatalytic treatment processes. Therefore, the PPS/PVA/Fe_3O_4/AgNPs nanocomposite was subjected to successive photocatalytic cycles for the degradation of methyl orange (MO) to evaluate its stability and reusability. After each cycle, the photocatalyst was recovered, washed with ethanol and deionized water, and dried at 40 °C for 24 h before being reused in a fresh MO solution under the same photocatalytic conditions.

As shown in Fig. 12, the photocatalytic degradation efficiency decreased from approximately 91% in the first cycle to 86% after the fourth cycle, corresponding to a decrease of about 5 percentage points. The relatively small decrease indicates that the nanocomposite retained a substantial portion of its photocatalytic activity over the four consecutive cycles. The observed decrease may be associated with partial occupation or blockage of accessible surface sites by residual dye molecules or transformation products remaining after each cycle. In addition, the loss of a small fraction of the catalyst during the recovery, washing, and transfer procedures may have contributed to the decrease in activity [29].

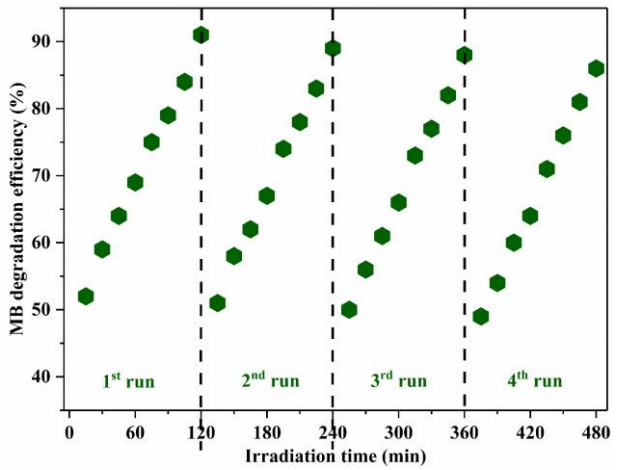

Fig. 12: Reusability analysis of the PPS/PVA/Fe_3O_4/AgNPs over four cycles.

Overall, the PPS/PVA/Fe_3O_4/AgNPs nanocomposite maintained relatively stable photocatalytic performance over four consecutive cycles under the applied experimental conditions. These results demonstrate that the nanocomposite retained a substantial portion of its photocatalytic activity during the four-cycle test and provide preliminary evidence of its reusability under the investigated conditions. However, evaluation of long-term stability and practical applicability would require a larger number of reuse cycles and, preferably, characterization of the catalyst before and after repeated use to assess possible changes in its structural, morphological, and compositional properties.

The incorporation of Fe_3O_4 also provides magnetic responsiveness to the nanocomposite, which may facilitate catalyst recovery from aqueous media using an external magnetic field [25]. However, direct magnetic separation was not evaluated in the present study; therefore, the potential advantage of magnetic recovery should be considered a prospective feature rather than an experimentally demonstrated recovery method.

4. Conclusion

In this study, a PPS/PVA/Fe_3O_4/AgNPs nanocomposite was prepared by a simple co-precipitation method and evaluated as a visible-light-responsive photocatalyst for the degradation of methyl orange (MO) in aqueous solution. The characterization results supported the incorporation of the polymeric and inorganic components within the nanocomposite, while BET analysis indicated a substantial increase in the specific surface area from 1.52 $m^2\ g^{-1}$ for pure PPS to 26.68 $m^2\ g^{-1}$ for the nanocomposite after incorporation of PVA, Fe_3O_4, and AgNPs.

Under the applied experimental conditions, the PPS/PVA/Fe_3O_4/AgNPs nanocomposite achieved approximately 91% MO degradation after 120 min of visible-light irradiation, with an apparent pseudo-first-order rate constant of 9.1 × 10^{-3} min^{-1}. The enhanced photocatalytic performance of the nanocomposite compared with the individual and partially combined components may be associated with the combined effects of its structural, surface, and interfacial characteristics. The increased surface area may provide more accessible sites for interaction with MO, while the presence of Fe_3O_4 and AgNPs may contribute to interfacial charge-transfer processes and visible-light-induced photocatalytic activity. However, the exact charge-transfer pathway cannot be conclusively established from the present data alone.

Scavenger experiments suggested the involvement of multiple reactive species, with hydroxyl-radical-related processes showing the strongest inhibition under the investigated conditions, while superoxide-related species also appeared to contribute to MO degradation. The reusability experiments demonstrated that the photocatalyst retained a substantial portion of its activity over four consecutive cycles, with the degradation efficiency decreasing from approximately 91% in the first cycle to 86% in the fourth cycle.

The Fe_3O_4 component also provides magnetic responsiveness, which may offer an advantage for catalyst recovery from aqueous media using an external magnetic field. Nevertheless, direct magnetic separation and long-term structural stability were not investigated in the present study. Overall, the obtained results demonstrate the potential of the PPS/PVA/Fe_3O_4/AgNPs nanocomposite for visible-light-assisted treatment of MO-containing aqueous solutions under the investigated laboratory conditions. Further studies involving extended reuse cycles, identification of degradation intermediates, mineralization assessment, catalyst characterization before and after reuse, and experiments with real wastewater are required to further evaluate its stability, mechanism, and practical environmental applicability.

References

[1] M. T. Rahaman, A. D. Pranta, M. R. Repon, M. S. Ahmed, T. Islam, Green production and consumption of textiles and apparel: Importance, fabrication, challenges and future prospects, *J. Open Innov.*, 10 (2024) 100280.

[2] M. Taghdiri, F. Ghanei, M. Ardakani, H. Banitaba, H. Aarabi Ardakani, Hybridization of phosphomolybdic acid with hexamine and hexamine-nickel for improving of activity in photodegradation of dyes under sunlight irradiation, *Iran. J. Anal. Chem.*, 8 (2021) 80–89.

[3] J. Prakash, P. Kumar, N. Saxena, Z. Pu, Z. Chen, A. Tyagi, G. Zhang, S. Sun, CdS based 3D nano/micro-architectures: Formation mechanism, tailoring of visible light activities and emerging applications in photocatalytic H_2 production, CO_2 reduction and organic pollutant degradation, *J. Mater. Chem. A*, 11 (2023) 10015–10064.

[4] N. Kumar, R. Gusain, S. Pandey, S. S. Ray, Hydrogel nanocomposite adsorbents and photocatalysts for sustainable water purification, *Adv. Mater. Interfaces*, 10 (2023) 2201375.

[5] P. G. Ghamari Kargar, M. Hosseini, Visible-light photocatalytic conversion of fructose to 5-HMF

and 5-EMF using a deep eutectic solvent-assisted Fe_3O_4@g-CN-DA-SO_3H nanohybrid, *Inorg. Chem. Commun*., 186 (2026) 116156.

[6] M. M. Sadughi, M. Hosseini, K. Gallardo, Next-generation nanophotocatalyst for ultra-efficient and sustainable azithromycin decontamination: A breakthrough strategy for visible-light-driven pharmaceutical waste treatment, *Top. Catal*., 69 (2026) 724–739.

[7] M. Hosseini, Visible-light-assisted decontamination of sertraline in water using a Co_3O_4/g-C_3N_4 nanocomposite photocatalyst, *Environ. Sci. Pollut. Res*., 32 (2025) 20441–20460.

[8] M. Hosseini, M. Panahimehr, S. M. Khoshfetrat, Solar-driven clopidogrel degradation with europium-enhanced ZnO nanocatalyst, *Int. J. Environ. Sci. Technol.*, 22 (2025) 9915–9932.

[9] M. Panahimehr, S. Asghari, M. Hosseini, A. Mojaddami, Eco-friendly synthesis of magnetic Pd/$NiFe_2O_4$/chitosan nanobiocatalyst for enhanced degradation of Congo red dye under sunlight irradiation, *Results Chem*., 15 (2025) 102300.

[10] M. Panahimehr, S. Asghari, M. Hosseini, A. Mojaddami, Pd/$ZnMn_2O_4$/chitosan nanobiocatalyst: A sustainable solution for sunlight-enhanced photocatalytic degradation of Congo red dye, *J. Mol. Struct*., 1347 (2025) 143339.

[11] S. Husain, A. Nandi, F. Z. Simnani, U. Saha, A. Ghosh, A. Sinha, A. Sahay, S. K. Samal, P. K. Panda, S. K. Verma, Emerging trends in advanced translational applications of silver nanoparticles: A progressing dawn of nanotechnology*, J. Funct. Biomater*., 14 (2023) 47.

[12] X. Deng, D. Alfonso, T.-D. Nguyen-Phan, D. R. Kauffman, Resolving the size-dependent transition between CO_2 reduction reaction and H_2 evolution reaction selectivity in sub-5 nm silver nanoparticle electrocatalysts, *ACS Catal*., 12 (2022) 5921–5929.

[13] L. S. Montagna, M. Y. Kondo, E. S. Callisaya, C. Mello, B. R. Souza, A. P. Lemes, E. C. Botelho, M. L. Costa, M. C. S. Alves, M. V. Ribeiro, M. C. Rezende, A review on research, application, processing, and recycling of PPS based materials, *Polímeros*, 32 (2022) e2022005.

[14] Y. Fan, H. Ben, L. Li, A novel metal-free photocatalyst polyphenylene sulfide: Synthesis, characterization and performance evaluation, *Appl. Catal. B*, 274 (2020) 119073.

[15] C. Yang, N. Han, W. Zhang, Adhesive-free in situ synthesis of a coral-like titanium dioxide@poly(phenylene sulfide) microporous membrane for visible-light photocatalysis, *Chem. Eng. J*., 374 (2019) 1382–1393.

[16] M. Atashkadi, A. Mohadesi, M. A. Karimi, S. Z. Mohammadi, V. H. Aghaei, Preparation, characterization, and application of novel ternary PPS/PVA/Fe_3O_4 nanocomposite for enhanced visible light photocatalytic degradation of methylene blue, *J. Cluster Sci*., 35 (2024) 497–518.

[17] International Organization for Standardization, Particle size analysis—Dynamic light scattering (DLS), ISO 22412:2025, ISO (2025).

[18] M. Chatterjee, A. Ghosh, A. Mondal, D. Banerjee, Polyaniline–single walled carbon nanotube composite—a photocatalyst to degrade rose bengal and methyl orange dyes under visible-light illumination, *RSC Adv*., 7 (2017) 36403–36415.

[19] B. Cui, H. Cui, Z. Li, H. Dong, X. Li, L. Zhao, J. Wang, Novel $Bi_3O_5I_2$ hollow microsphere and its enhanced photocatalytic activity, *Catalysts*, 9 (2019) 709.

[20] A. R. Upreti, Y. Li, N. Khadgi, S. Naraginti, C. Zhang, Efficient visible light photocatalytic degradation of 17α-ethinyl estradiol by a multifunctional Ag–AgCl/$ZnFe_2O_4$ magnetic nanocomposite, *RSC Adv*., 6 (2016) 32761–32769.

[21] R. Majumdar, P. K. Kar, Biosynthesis, characterization and anthelmintic activity of silver nanoparticles of Clerodendrum infortunatum isolate*, Sci. Rep*., 13 (2023) 7415.

[22] J. S. J. Hargreaves, Some considerations related to the use of the Scherrer equation in powder X-ray diffraction as applied to heterogeneous catalysts, Catal. *Struct. React*., 2 (2016) 33–37.

[23] V. Tong, K. Mingard, Measurement uncertainties of energy dispersive X-ray spectroscopy in the scanning electron microscope (SEM-EDX/EDS), NPL Report MAT 135, *National Physical Laboratory* (2026).

[24] G. Chen, H. Yang, X. Zhang, J. Liu, J. Tang, Clarification of the magnetocapacitance mechanism for Fe_3O_4-PDMS nanocomposites, *J. Nanomater*., 2015 (2015) 982174.

[25] W. Wu, C. Jiang, V. A. L. Roy, Recent progress in magnetic iron oxide–semiconductor composite nanomaterials as promising photocatalysts, *Nanoscale*, 7 (2015) 38–58.

[26] M. Thommes, K. Kaneko, A. V. Neimark, J. P. Olivier, F. Rodriguez-Reinoso, J. Rouquerol, K. S. W. Sing, Physisorption of gases, with special reference to the evaluation of surface area and pore size distribution (IUPAC Technical Report), *Pure Appl. Chem*., 87 (2015) 1051–1069.

[27] H. D. Tran, D. Q. Nguyen, P. T. Do, U. N. P. Tran, Kinetics of photocatalytic degradation of organic compounds: A mini-review and new approach, *RSC Adv*., 13 (2023) 16915–16925.

[28] H. Chaker, L. Chérif-Aouali, S. Khaoulani, A. Bengueddach, S. Fourmentin, Photocatalytic degradation of methyl orange and real wastewater by silver doped mesoporous TiO_2 catalysts, *J. Photochem. Photobiol. A Chem*., 318 (2016) 142–149.

[29] M. Arif, Catalytic reduction/degradation of methyl orange by metal nanoparticle containing systems: A critical review, *RSC Adv*., 15 (2025) 27668–27684.

https://ijac.journals.pnu.ac.ir/

نشریه ایرانی شیمی تجزیه

سال سیزدهم، شماره یکم، بهار ۱۴۰۵، صفحات ۱۵۱-۱۷۲

DOI: 10.30473/ijac.2026.80202.1364

دسترسی آزاد

مقاله پژوهشی

بهبود عملکرد فوتوکاتالیستی نانوکامپوزیت PPS/PVA/Fe$_3$O$_4$/AgNPs برای تجزیهٔ کارآمد متیل اورانژ

اکرم افشاری کاوه[۱]، شیدا احمدی[۲*]

۱. دانشجوی دکترا، گروه شیمی، دانشگاه پیام نور، تهران، ایران.

۲. دانشیار، گروه شیمی، دانشگاه پیام نور، تهران، ایران.

نویسنده مسئول:
شیدا احمدی
رایانامه: sh.ahmadi_ch@pnu.ac.ir

تاریخ دریافت: ۱۴۰۵/۰۸/۲۰
تاریخ پذیرش: ۱۴۰۵/۰۸/۲۳

استناد به این مقاله:
افشاری کاوه، اکرم و احمدی، شیدا. (۱۴۰۵). بهبود عملکرد فوتوکاتالیستی نانوکامپوزیت PPS/PVA/Fe$_3$O$_4$/AgNPs برای تجزیهٔ کارآمد متیل اورانژ. *نشریه ایرانی شیمی تجزیه*، ۱۳(۱) ۱۵۱-۱۷۲.
(DOI:10.30473/ijac.2026.80202.1364)

چکیده

در این پژوهش، نانوکامپوزیت PPS/PVA/Fe$_3$O$_4$/AgNPs با استفاده از یک روش ساده هم‌رسوبی تهیه شد و به‌عنوان یک فتوکاتالیست پاسخ‌گو به نور مرئی برای تجزیه متیل اورانژ (MO) در محلول آبی مورد بررسی قرار گرفت. مواد تهیه‌شده با استفاده از پراش پرتو ایکس (XRD)، طیف‌سنجی مادون قرمز تبدیل فوریه (FT-IR)، طیف‌سنجی پراش انرژی پرتو ایکس (EDX)، مغناطیس‌سنجی نمونه ارتعاشی (VSM)، آنالیز برونر–امت–تلر (BET)، میکروسکوپ الکترونی روبشی گسیل میدانی (FESEM) و پراکندگی نور دینامیکی (DLS) مشخصه‌یابی شدند. تصاویر FESEM برای ارزیابی کیفی مورفولوژی سطح استفاده شدند، و DLS نیز برای اندازه‌گیری قطر هیدرودینامیکی نمونه‌ها در سوسپانسیون به کار رفت. سطح ویژه BET از ۱/۵۲ مترمربع بر گرم برای PPS به ۲۶/۶۸ مترمربع بر گرم برای نانوکامپوزیت PPS/PVA/Fe$_3$O$_4$/AgNPs افزایش یافت. تحت شرایط آزمایشی مورد استفاده، نانوکامپوزیت پس از ۱۲۰ دقیقه تابش نور مرئی، حدود ۹۱ درصد تجزیه MO را نشان داد و ثابت سرعت ظاهری شبه‌مرتبه اول (kapp) برابر با ۳-۱۰ × ۹/۱ بردقیقه به دست آمد. نتایج آزمایش‌های مهارکننده (scavenger) نشان‌دهنده مشارکت چندین گونه فعال در فرایند تجزیه بود و بیشترین میزان مهار در حضور ایزوپروپانول مشاهده شد که بیانگر مشارکت مهم فرایندهای مرتبط با رادیکال‌های هیدروکسیل استفعالیت فتوکاتالیستی نانوکامپوزیت طی چهار چرخه متوالی حفظ شد. همچنین، نانوکامپوزیت حاوی Fe$_3$O$_4$ رفتار مغناطیسی قابل‌توجهی نشان داد.که پتانسیل آن را برای بازیابی کاتالیزور از محلول تأیید می‌کند. در مجموع، نتایج این مطالعه پتانسیل نانوکامپوزیت PPS/PVA/Fe$_3$O$_4$/AgNPs را برای تجزیه مؤثر متیل اورانژ (MO) تحت تابش نور مرئی، در شرایط آزمایشگاهی بررسی‌شده، نشان می‌دهد.

واژه‌های کلیدی

فتوکاتالیز، نانوکامپوزیت، متیل اورانژ، تجزیه، نانوذرات نقره (AgNPs).

حق انتشار این مستند، متعلق به نویسندگان آن است. ۱۴۰۵ ©. ناشر این مقاله، دانشگاه پیام نور است.

این مقاله تحت گواهی زیر منتشرشده و هر نوع استفاده غیرتجاری از آن مشروط بر استناد صحیح به مقاله و با رعایت شرایط مندرج در آدرس زیر مجاز است.
Creative Commons Attribution-NonCommercial 4.0 International license (https://creativecommons.org/licenses/by-nc/4.0/)